

Appendices for “Extreme events and non-Kolmogorov -5/3 spectra in turbulent flows behind two side-by-side square cylinders”

Yi Zhou^{1†}, Koji Nagata², Yasuhiko Sakai³, and Tomoaki Watanabe²

¹School of Energy and Power Engineering, Nanjing University of Science and Technology, Nanjing 210094, China

²Department of Aerospace Engineering, Nagoya University, Nagoya 464-8603, Japan

³Department of Mechanical Science and Engineering, Nagoya University, Nagoya 464-8603, Japan

Appendix A. Verification of the numerical strategies

In this study, the immerse boundary method, which could possibly introduce non-physical contaminations in the near-wake field, is adopted. One would argue that the immersed boundary method can lead to inaccurate prediction of the near-wall dynamics. Also, it is hard to fully resolve the near-wall boundary layer (i.e. viscous sublayer) by current state-of-the-art DNS. Thus, we need to compare our DNSs against previous studies for validation. However, there are few experimental and numerical data available, if not none, with which we could directly compare our simulation results of dual-wake flow. In contrast, lots of numerical or experimental investigations of turbulent flows past a bluffbody (i.e. single square cylinder) have been carried out. To further validate our simulation strategies, therefore, we perform an extra direct numerical simulation on the wake behind a single square cylinder, which is actually a basic element of the arrays of cylinders considered and access various statistics against both numerical and experimental data. Note that except for the numbers of the mesh nodes and the resulting size of the simulation domain, the other geometrics parameters (e.g. inlet Reynolds number, streamwise thickness, distributions of mesh sizes, namely, resolutions ΔX , ΔY and ΔZ) and simulation settings (e.g. spatial and temporal discretization schemes, immerse boundary method and boundary conditions) are the exactly same as those in the simulations of dual-wake flows. The details of the verification simulation are given in Table 1.

Despite the scatter in the reported experimental and numerical results, it can be seen from figure 1 that the streamwise evolutions of various velocity statistics (i.e. U_C , U_{rms} , U_{rms} and W_{rms}) along the centreline are roughly in accord with those in previous studies. To further investigate the fluid dynamics on the solid surfaces, the distributions of the pressure coefficient $C_p = 2 \frac{(P - P_{in})}{(\rho U_{in}^2)}$ on four sides of the square cylinder, where ρ and P_{in} denote flow density and inlet mean pressure, respectively, are plotted in figure 2. Again our pressure data are in good agreement with previous investigations. Both figures 1 and 2 confirm that the numerical results of a single wake are in close agreement with those in previous both experimental and numerical studies. Considering the fact that in the cases of wake-interactions virtually the same numerical strategies and parameters are

† Email address for correspondence: yizhou@njust.edu.cn

Case	Re_{T_0}	L_d/T_0	X_{bar}/T_0	L_X/T_0	L_Y/T_0	L_Z/T_0	N_X	N_Y	N_Z	$\Delta t/(T_0/U_{in})$
WF	2500	6	8	35	15	5	801	346	100	0.0045

TABLE 1. Geometric and numerical details of the validation simulation

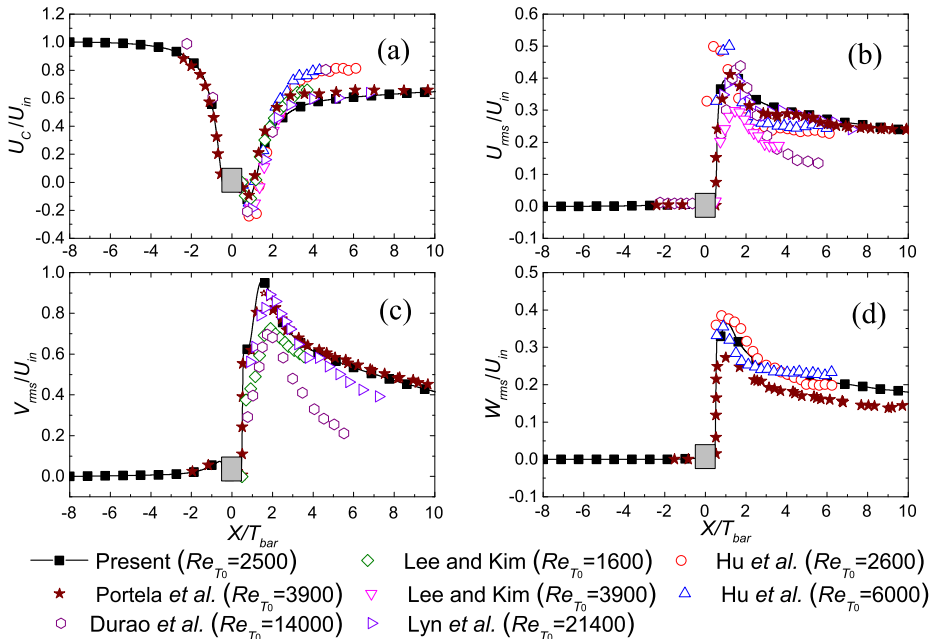


FIGURE 1. Centreline evolutions of (a) U_C/U_{in} ; (b) U_{rms}/U_{in} ; (c) V_{rms}/U_{in} and (d) W_{rms}/U_{in} in the turbulent flow behind a single square cylinder. The corresponding data from previous experiments by Lee & Kim (2001*a,b*), Hu, Zhou & Dalton (2006), Lyn *et al.* (1995) and Durao, Heitor & Pereira (1988) (denoted by open symbols) and simulation by Portela, Papadakis & Vassilicos (2017) (denoted by filled symbols) are also plotted for comparison.

adopted, we may safely draw the conclusion that our DNS results in the main text are reliable.

Appendix B. Confinement effects imposed by domain size

In § 2, we demonstrate that the ratios of L_Y/b meet the criterion introduced by Redford, Castro & Coleman (2012) for all three cases considered ($L_d/T_0 = 4, 6$ and 8). To further investigate the possible confinements proposed by the domain size, the streamwise evolutions of $T_0/U_{in}dU/dx(x, 1/2L_Y)$ and $M = \int_{-1/2L_Y}^{1/2L_Y} U^2 dy$ are plotted in figure 3 for all three cases. The values of the x derivative of the mean streamwise velocity at the domain boundary (i.e. $Y/L_Y = 1/2$) for all three cases are considerably smaller in the downstream region (below approximately $U_{in}/T_0 \times 10^{-4}$). A non-negligible variable of the mean velocity U is detected in the upstream region, which is associated with the corresponding large velocity deficit imposed by the solid bars. With increasing distance, however, the derivative of the mean velocity U at the boundary (i.e. $Y = 1/2L_Y$) continually decreases. A similar observation about the derivative of U at the domain edge was already reported in Dairay, Obligado & Vassilicos (2015). It is well-established that in

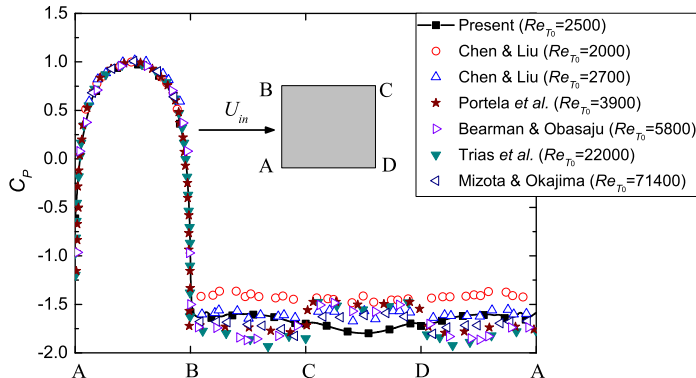


FIGURE 2. Distributions of the mean pressure coefficient C_p over the four sides (i.e. $A-B$, $B-C$, $C-D$ and $D-A$ sides) of the single square cylinder. The open symbols correspond to experimental data (Chen & Liu 1999; Bearman & Obasaju 1982; Mizota & Okajima 1981), whereas the filled symbols denote numerical data (Portela *et al.* 2017; Trias, Gorobets & Oliva 2015).

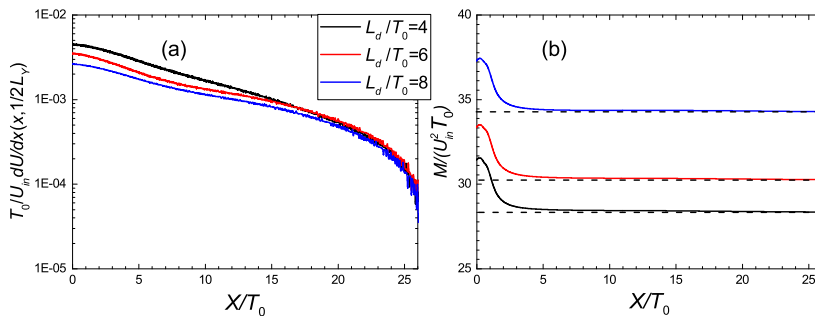


FIGURE 3. Streamwise evolution of (a) $T_0/U_{in}dU/dx(x, 1/2L_Y)$ and (b) $M/U_{in}^2T_0$ for all three cases considered.

Case	Re_{T_0}	L_d/T_0	X_{bar}/T_0	L_X/T_0	L_Y/T_0	L_Z/T_0	N_X	N_Y	N_Z	$\Delta t/(T_0/U_{in})$
WI6L	2500	6	8	35	48	5	801	1104	100	0.0045

TABLE 2. Geometric and numerical details of the auxiliary simulation case

the far shear flows, $M = \int_{-1/2L_Y}^{1/2L_Y} U^2 dy = \text{const}$. Figure 3(b) confirms that the momentum M is indeed well-conserved in the far-field.

Moreover, another simulation with a larger vertical size of the simulation domain (i.e. $L_Y/T_0 = 48$) is performed to quantitatively assess the influence of the boundary setting. Except for the size of the vertical size L_Y and the corresponding number N_Y , the other parameters of the auxiliary simulation are the same as those in the case WI6, as can be seen from Table 2. Figure 4 shows the vertical profiles of U_m/U_{in} at $X/T_0 = 26$ for the two different simulations. Although the velocities of the ambient flow at the boundaries (i.e. $Y/L_Y = \pm 1/2$) are somewhat different, the lateral sizes of the wakes are almost identical. This observation actually echoes our previous assertion that for the simulation with $L_Y/T_0 = 30$ the growth of the wakes is unlikely to be suppressed by the constrain proposed by the simulation domain. Figure 5 show the centreline evolutions of the mean streamwise velocity and the rms velocity, where it can be clearly seen that the influences

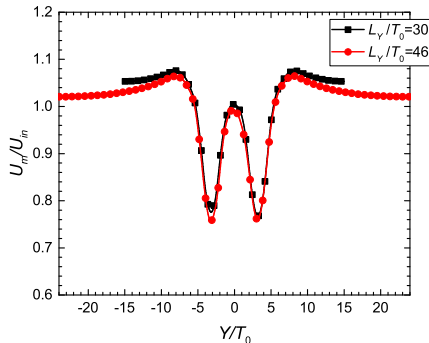


FIGURE 4. Vertical distribution of U_m/U_{in} at a far downstream location (i.e. $X/T_0 = 26$) for the two simulations with different vertical sizes (i.e. $L_Y/T_0 = 30$ and $L_d/T_0 = 46$).

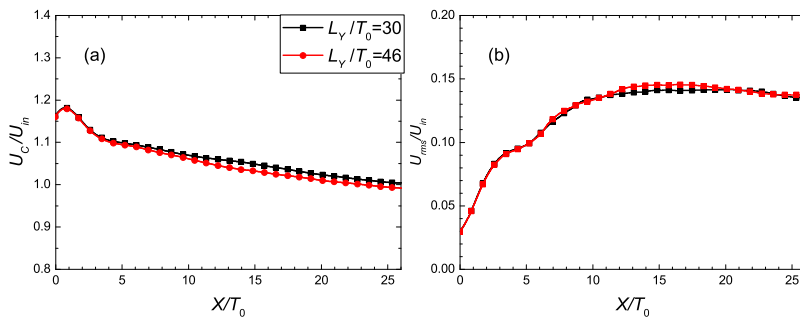


FIGURE 5. Streamwise evolution of (a) the normalized mean velocity U_C/U_{in} and (b) the normalized rms velocity U_{rms}/U_{in} along the centreline.

of the domain size on the centreline statistics are considerably small. Finally, we may safely draw the conclusion that the confinement effects are weak.

Appendix C. Statistical convergence

The statistics are averaged over 2×10^5 time steps (or equivalently 128 vortex shedding periods) and the quasi-homogeneous Z direction. Owing to the strong vortex shedding in the near field region (e.g. $X/T_0 = 6$), it can be highly demanding to secure adequate statistical convergence of the second-order structure function $\langle \delta u'^2(\Delta t) \rangle$. One could argue that the absence of the $2/3$ power-law may stem from the lack of the statistical convergence. Consequently, it becomes necessary to compute the second-order structure function based on different selections of time steps to confirm that the exponents of $\langle \delta u'^2(\Delta t) \rangle$ are indeed independent of time steps used in the average (or possess a weak dependence on the number of time steps). Figure 6 shows the second-order structure function $\langle \delta u'^2(\Delta t) \rangle$ at $X/T_0 = 6$ along the centreline by using different numbers of time steps (i.e. $N_s = 4 \times 10^4$, 1.2×10^5 and 2×10^5). It is clear that the peak values of $\langle \delta u'^2(\Delta t) \rangle$ are not exactly the same, indicating a lack of full convergence. However, for all three time steps the exponents of $\langle \delta u'^2(\Delta t) \rangle$ are quite similar to each other, that is, the appearance of the large power-law exponent 1 is independent of the lack of convergence.

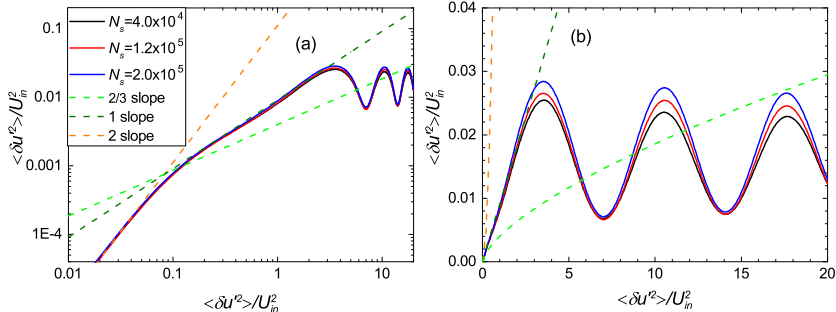


FIGURE 6. Second-order structure function $\langle \delta u'^2(\Delta t) \rangle$ at $X/T_0 = 6$ along the centreline corresponding to different time steps (i.e. $N_s = 4 \times 10^4$, 1.2×10^5 and 2×10^5) and averaged over Z direction for the case with $L_d/T_0 = 6$. (a) shown on a logarithmic-logarithmic scale; (b) shown on a linear-linear scale. The dashed lines corresponds to functions with different power-law exponents (i.e. 2/3, 1 and 2).

Appendix D. Verification of the filtering processes

By decomposing the full streamwise velocity fluctuation u' into three different components, the corresponding decomposition in the form of the Fourier series is

$$u'(t) = u'_>(t) + u'_\sim(t) + u'_<(t) = \sum_{f > f_h} \hat{c}_f e^{ift} + \sum_{f_1 < f < f_h} \hat{c}_f e^{ift} + \sum_{f < f_1} \hat{c}_f e^{ift}. \quad (\text{D1})$$

Substituting $u'(t) = u'_>(t) + u'_\sim(t) + u'_<(t)$ into the second-order structure function $\langle \delta u'^2(\Delta t) \rangle$ yields

$$\begin{aligned} \langle (u'(t + \Delta t) - u'(t))^2 \rangle &= \langle \delta u'^2_{>}(\Delta t) + \delta u'^2_{\sim}(\Delta t) + \delta u'^2_{<}(\Delta t) \\ &\quad + 2(u'_{>}(t + \Delta t) - u'_{>}(t))(u'_{\sim}(t + \Delta t) - u'_{\sim}(t)) \\ &\quad + 2(u'_{>}(t + \Delta t) - u'_{>}(t))(u'_{<}(t + \Delta t) - u'_{<}(t)) \\ &\quad + 2(u'_{\sim}(t + \Delta t) - u'_{\sim}(t))(u'_{<}(t + \Delta t) - u'_{<}(t)). \end{aligned} \quad (\text{D2})$$

The decomposition of the fourth term on the right-hand of the above equation is

$$\begin{aligned} 2\langle (u'_{>}(t + \Delta t) - u'_{>}(t))(u'_{\sim}(t + \Delta t) - u'_{\sim}(t)) \rangle &= 2\langle u'_{>}(t + \Delta t)(u'_{\sim}(t + \Delta t)) \rangle \\ &\quad - 2\langle u'_{>}(t + \Delta t)u'_{\sim}(t) \rangle - 2\langle u'_{>}(t)u'_{\sim}(t + \Delta t) \rangle + 2\langle u'_{>}(t)u'_{\sim}(t) \rangle. \end{aligned} \quad (\text{D3})$$

Parseval's identity implies that $\langle g(t)h(t) \rangle = \sum_f \hat{g}_f \hat{h}_{-f}$, where $g(t) = \sum_f \hat{g}_f e^{ift}$ and $h(t) = \sum_f \hat{h}_f e^{ift}$. Considering decomposition of the velocity components in the form of the Fourier series (see Eq. (B1)), for the production terms on the right-hand of Eq. (B3) the corresponding interact of the Fourier component sets is always empty. Consequently, the productions of the filtered functions in Eq.(B3) are orthogonal, i.e. $\langle u'_{>}(t + \Delta t)u'_{\sim}(t + \Delta t) \rangle = \langle u'_{>}(t + \Delta t)u'_{\sim}(t) \rangle = \langle u'_{>}(t)u'_{\sim}(t + \Delta t) \rangle = \langle u'_{>}(t)u'_{\sim}(t) \rangle = 0$. Similarly, the fifth and sixth terms on the right-hand of Eq. (B2) also vanish, leading to the following relation:

$$\langle \delta u'^2(\Delta t) \rangle = \langle \delta u'^2_{<}(\Delta t) \rangle + \langle \delta u'^2_{\sim}(\Delta t) \rangle + \langle \delta u'^2_{>}(\Delta t) \rangle. \quad (\text{D4})$$

Similarly, one can also prove that

$$\langle \delta u'^2_{\sim}(\Delta t) \rangle = \langle \delta u'^2_{\sim,i}(\Delta t) \rangle + \langle \delta u'^2_{\sim,h}(\Delta t) \rangle. \quad (\text{D5})$$

In § 4, the full streamwise velocity fluctuation u' is decomposed into three different

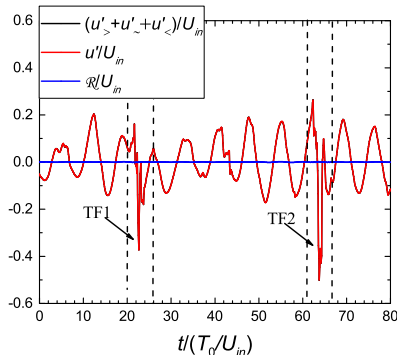


FIGURE 7. Time-traces of the sum of the filtered signals $(u'_> + u'_~ + u'_<)/U_{in}$, the full signals u'/U_{in} and the resulting residual term \mathcal{R}/U_{in} .

components (i.e. $u'_>$, $u'_~$ and $u'_<$ corresponding, respectively, to low-, intermediate- and high-frequency components). The lower cutoff and higher cutoff frequencies are 0.2 and 0.8, respectively. In our work, high-order bidirectional Butterworth filters are adopted, which could efficiently remove the undesired components and the wanted frequency ranges remain virtually intact as shown in figures 12(a)–15(a) in the main text.

Figure 7 shows the time-traces of the full signals u'/U_{in} , the sum of the filtered components $(u'_> + u'_~ + u'_<)/U_{in}$ and the residual balance \mathcal{R}/U_{in} . The profiles of u'/U_{in} and $(u'_> + u'_~ + u'_<)/U_{in}$ are close enough to be collapsed together. Furthermore, including in the TF1 and TF2, the magnitude of \mathcal{R}/U_{in} within the whole time frame plotted is considerably small, lending further credence to the filters used.

The main conclusion reached in this work concerning the appearance of the $-5/3$ scaling law and the extreme events strongly depend on the filtering process. Obviously, for computation the full velocity fluctuation u' can be expressed in the form of

$$u' = u'_> + u'_~ + u'_< + \mathcal{R}, \quad (\text{D } 6)$$

where \mathcal{R} is the residual balance term, which allows us to further evaluate the filtering process (i.e. the level of signal delay and distortion introduced by the filters). The three velocity components $u'_>$, $u'_~$ and $u'_<$, are orthogonal to each other. Therefore, if high-fidelity filters are used, we could have the relation $\langle \delta u'^2(\Delta t) \rangle = \langle \delta u'^2_{<}(\Delta t) \rangle + \langle \delta u'^2_{~}(\Delta t) \rangle + \langle \delta u'^2_{>}(\Delta t) \rangle$. For a final assessment of the quality of the filters chosen, we examine $\langle \delta u'^2(\Delta t) \rangle / U_{in}^2$ and $\langle \delta u'^2_{<}(\Delta t) + \delta u'^2_{~}(\Delta t) + \delta u'^2_{>}(\Delta t) \rangle / U_{in}^2$ versus $\Delta t U_{in} / T_0$ at $X/T_0 = 6$ and 26. Very close balances between $\langle \delta u'^2(\Delta t) \rangle / U_{in}^2$ and $\langle \delta u'^2_{<}(\Delta t) + \delta u'^2_{~}(\Delta t) + \delta u'^2_{>}(\Delta t) \rangle / U_{in}^2$ at $X/T_0 = 6$ and 26 are reached (for economy of space not shown herein).

REFERENCES

- BEARMAN, P. W. & OBASAJU, E. D. 1982 An experimental study of pressure fluctuations on fixed and oscillating square-section cylinders. *J. Fluid Mech.* **119**, 297–321.
- CHEN, J. M. & LIU, C. H. 1999 Vortex shedding and surface pressures on a square cylinder at incidence to a uniform air stream. *Int. J. Heat Fluid Flow* **20**, 592–597.
- DAIRAY, T., OBLIGADO, M. & VASSILICOS, J. C. 2015 Non-equilibrium scaling laws in axisymmetric turbulent wakes. *J. Fluid Mech.* **781**, 166–195.
- DURAO, D. F. G., HEITOR, M. V. & PEREIRA, J. C. F. 1988 Measurements of turbulent and periodic flows around a square cross-section cylinder. *Exp. Fluids* **6**, 298–304.
- HU, J. C., ZHOU, Y. & DALTON, C. 2006 Effects of the corner radius on the near wake of a square prism. *Exp. Fluids* **40**, 106–118.

- LEE, M. & KIM, G. 2001*a* A study on the near wake of a square cylinder using particle image velocimetry (I) - Mean flow (in Korean). *Trans. Korean Soc. Mech. Engng* **25**, 1408–1416.
- LEE, M. & KIM, G. 2001*b* A study on the near wake of a square cylinder using particle image velocimetry (II) - Turbulence characteristics (in Korean). *Trans. Korean Soc. Mech. Engng* **25**, 1417–1426.
- LYN, D. A., EINAV, S., RODI, W. & PARK, J. H. 1995 A laser-doppler velocimetry study of ensemble-averaged characteristics of the turbulent near wake of a square cylinder. *J. Fluid Mech.* **304**, 285–319.
- MIZOTA, T. & OKAJIMA, A. 1981 Experimental studies of time mean flows around rectangular prisms (in Japanese). *Proc. Japan Soc. Civ. Engrs* **312**, 39–47.
- PORTELA, F. A., PAPADAKIS, G. & VASSILICOS, J. C. 2017 The turbulence cascade in the near wake of a square prism. *J. Fluid Mech.* **825**, 315–352.
- REDFORD, J. A., CASTRO, I. P. & COLEMAN, G. N. 2012 On the universality of turbulent axisymmetric wakes. *J. Fluid Mech.* **710**, 419–452.
- TRIAS, F. X., GOROBETS, A. & OLIVA, A. 2015 Turbulent flow around a square cylinder at reynolds number 22,000: A DNS study. *J. Fluid Mech.* **123**, 87–98.